OPEN ACCESS

Progress in the Cycling Performance of Oxidic Solid-State Batteries Fabricated at Room Temperature by Powder Aerosol Deposition

To cite this article: Lukas Hennerici *et al* 2026 *J. Electrochem. Soc.* **173** 040517

Journal of The Electrochemical Society, 2026 **173** 040517

Progress in the Cycling Performance of Oxidic Solid-State Batteries Fabricated at Room Temperature by Powder Aerosol Deposition

Lukas Hennerici,[1,2,z] Dominik Bröse,[1] Maximilian Schamel,[2,3] Sabrina Lang,[4] Paula Ficht,[1] Dominik Kramer,[4] Reiner Mönig,[4] Michael A. Danzer,[2,3] and Ralf Moos[1,2]

[1]*Department of Functional Materials, University of Bayreuth, Universitätsstraße 30, 95447 Bayreuth, Germany*
[2]*Bavarian Center for Battery Technology (BayBatt), University of Bayreuth, Weiherstraße 26, 95448 Bayreuth, Germany*
[3]*Chair of Electrical Energy Systems, University of Bayreuth, Universitätsstraße 30, 95447 Bayreuth, Germany*
[4]*Institute of Applied Materials, Karlsruhe Institute of Technology, Herrmann-von-Helmholtz-Platz 1, 76344 Eggenstein-Leopoldshafen, Germany*

The fabrication of solid-state batteries (SSBs) without the need for high-temperature sintering significantly requires less energy. The powder aerosol deposition (PAD) method enables direct film formation at room temperature, bypassing the conventional thermal densification step. This study presents an overview of recent advancements in the cycling properties of SSBs fabricated via PAD. Employing $LiNi_{0.82}Mn_{0.07}Co_{0.11}O_2$ (NMC) as cathode active material (CAM) and $Li_7La_3Zr_2O_{12}$ (LLZO) as solid electrolyte, a capacity of 141 mAh g^{-1} with 90 % capacity retention over 25 cycles is demonstrated with no thermal post-treatment applied after film fabrication. Based on these results, the role of LLZO as catholyte in the cathode layer is investigated. The findings suggest an electrochemical instability between nickel-rich NMC and LLZO during cycling. To enhance the capacity, the aggregated results are used to discuss various strategies for optimizing cathode layer design, particularly with respect to the composition and choice of the CAM.

 [DOI: 10.1149/1945-7111/ae4543]

Manuscript submitted December 11, 2025; revised manuscript received January 27, 2026. Published February 27, 2026.

Supplementary material for this article is available online

Lithium-ion batteries (LIB) employing liquid electrolytes are approaching their intrinsic limit in terms of achievable energy density.[1] To unlock the full potential of the lithium-ion technology, new cell concepts are required. Considerable research efforts have been directed toward the development of solid electrolytes (SEs) for the use both as electrolytes and catholytes, with the aim of replacing conventional liquid electrolytes in solid-state batteries (SSBs) as next-generation lithium-ion-batteries.[2–4]

One of the most promising candidates as SE material is the lithium-stuffed garnet-type oxide $Li_7La_3Zr_2O_{12}$ (LLZO). It combines high ionic conductivity of 10^{-3} S cm^{-1} with excellent chemical stability and a wide electrochemical operating window.[5–7] Currently, many resources are invested into tailoring the interface of LLZO toward active materials to decrease the interface resistance.[8–10]

However, an economic and environment-friendly processing method for the large-scale fabrication of LLZO electrolyte layers has yet to be established. Conventional processing methods such as tape-casting require a final sintering step at temperatures above 1000 °C to achieve dense films suitable for the application in SSBs.[11,12] Establishing a method that significantly reduces the required processing temperatures would therefore represent a major step towards sustainable and cost-effective cell fabrication.

Utilizing the powder aerosol deposition method (PAD, also referred to as aerosol deposition method (ADM) or vacuum kinetic spraying (VKS)) allows for the fabrication of dense (>95% of the bulk density) thick films already at room temperature in the thickness range from ca. 1 to 100 µm. Furthermore, no additional binder materials, which are not participating in the cell reactions during charging and discharging, are required for the deposition process.[13–17]

These process characteristics are advantageous not only for the fabrication of electrolyte layers but also for cathode layers. Eliminating dead volumes caused by binder materials allows for higher energy densities. Since PAD films are fully dense, their low porosity promotes good particle-to-particle contact reducing tortuosity.[13,16] This also extends to the fabrication of composite cathodes, i.e., to mixtures of cathode active material (CAM) and catholyte (SE). They are widely discussed in literature as a promising approach to ensure high ionic conductivity across all states of charge (SOC).[1,18–20]

Several studies have already investigated the properties of PAD-LLZO films[11,21–26] as well as PAD-cathodes films using widely applied CAMs such as $LiNi_{1-x-y}Mn_xCo_yO_2$ (NMC),[27–30] $LiCoO_2$ (LCO)[31–35] and $LiFePO_4$ (LFP).[36–38] However, only two studies have reported the combination of a PAD-fabricated cathode layer with a PAD-fabricated electrolyte layer extended with a manually applied lithium metal anode. For better readability, such a cell configuration will be referred to as "PAD-SSB" in the following. Ahn et al. demonstrated a PAD-SSB using a plain PAD-LFP cathode and a PAD-LLZO electrolyte layer.[39] More recently, we reported a PAD-SSB featuring an NMC/LLZO composite cathode layer in combination with an LLZO electrolyte layer.[13] While both studies provide a proof of concept, the obtained cell performances in terms of capacity and overall cell resistance do not meet the requirements for commercial application.

Consequently, to move forward, the aforementioned properties have to be improved. The aim of this study is to provide an overview of the current progress of the cycling performance of PAD-SSBs. The focus lies on evaluating the capacity during cycling. For the first time, PAD-SSBs incorporating nickel-rich NMC with the composition $LiNi_{0.82}Mn_{0.07}Co_{0.11}O_2$ as CAM are cycled over multiple cycles. The nickel-rich composition was selected due to its potential to deliver higher capacities. Furthermore, the influence of the catholyte fraction in composite cathodes — comprising nickel-rich NMC as CAM and LLZO as catholyte — on the aforementioned cycling performance is investigated. Based on the results, various approaches are discussed to enhance the cell characteristics of PAD-SSBs, particularly regarding capacity and charge carrier transport, aiming toward a more advanced and optimized cell design.

Experimental

Powder preparation.—NMC powder as CAM and LLZO powder as SE were obtained from industrial partners. The NMC powder was

[z]E-mail: functional.materials@uni-bayreuth.de

ball milled for 35 min in cyclohexane. After milling, the solvent was evaporated at room temperature. The powder was sieved using a mesh size of 90 μm, dried at 120 °C in a furnace, and stored in dry argon until further use. The LLZO powder was sieved using a mesh size of 90 μm in argon atmosphere and stored in dry argon until further use.

Powder mixtures for composite cathodes were prepared with compositions ranging from 90 wt-% (91 vol-%) to 10 wt% (11 vol-%) NMC and 10 wt-% (9 vol-%) to 90 wt-% (89 vol-%) LLZO. For this purpose, the respective powders were weighed, thoroughly mixed, and sieved using a 90 μm mesh. The mixing and sieving procedure was repeated once. The resulting powder mixtures were then stored under dry argon until further use.

Film fabrication.—All films used in this study were fabricated by PAD. Schematic illustrations of the PAD apparatus used are shown in Fig. 1. The principle of the PAD has previously been reported elsewhere.[11,13,15] Films used for XRD analysis were deposited on silicon wafers with (911) orientation (d_{Si} = 500 μm, CrysTec Kristalltechnologie, Berlin, Germany). Films used for ICP-OES, SEM, EDS and electrochemical characterization were fabricated on copper sheets (d_{Cu} = 500 μm). PAD-SSBs used for electrochemical characterization were fabricated by sequential deposition of cathode and electrolyte. 100 wt-% NMC, 70 wt-% (71 vol-%) NMC/30 wt-% (29 vol-%) LLZO (Composite A) or 40 wt-% (41 vol-%) NMC/60 wt-% (59 vol-%) LLZO (Composite B) were used as starting powder composition for the cathode composite layer fabrication.

In cases where a thermal annealing step was applied, the cathode layers were annealed prior to the deposition of the electrolyte layers. Thermal annealing at 400 °C for 1 h was performed in a custom-built tube furnace under inert N_2 atmosphere with heating and cooling rates of 1 K min^{-1}. All films were stored in an argon filled glovebox after the fabrication until further use.

The samples used to investigate the influence of thermal annealing on the electrochemical impedance of PAD-NMC films were prepared on an Al_2O_3 substrate equipped with a screen-printed four-wire contact structure. The samples were annealed in a custom-made purgeable furnace oven under N_2-atmosphere at different temperatures. Temperatures of 100 °C to 700 °C (in steps of 100 °C) were used with heating and cooling rates of 1 K min^{-1} as well as a dwell time of 1 h. After each annealing step, the samples were cooled to room temperature for EIS analyses.

Cell assembly.—To characterize the PAD-SSBs electrochemically, the surface of the PAD-LLZO layers were dry polished with sandpaper without an additive (1200 grit, SiC, 5 μm grain size) to remove unwanted residuals. Afterwards, lithium metal anodes (⌀ 3 mm, 0.75 mm thickness) were manually pressed on top of the covering PAD-LLZO layers resulting in a Cu|Cathode|LLZO|Li cell setup. The setup was extended with a manually applied copper current collector on top of the lithium metal anode. Finally, the samples were placed in a PAT-Cell (EL-Cell, Hamburg, Germany). A spring force of approximately 50 N (in accordance with data retrieved from the manufacturer, assuming an overall sample thickness of approximately 1.5 mm) resulting in an overall pressure of approximately 3 MPa was applied. The whole cell assembly until this point was performed in an argon filled glovebox. The PAT-Cell then was placed in a PAT-Stand-4 in a climate chamber under ambient atmosphere, maintaining a constant temperature of 70 °C during the individual characterization steps.

X-ray diffraction.—Pristine NMC and LLZO powders as well as deposited PAD-NMC films, PAD-Composite A films and PAD-Composite B films were analyzed by a StadiMP (STOE & Cie GmBH, Darmstadt, Germany) with a molybdenum anode operated at 3 kW, a Ge-Kα1-monochromator (λ = 1.5406 Å) and a silicon strip detector MYTHEN2 2 K (Dectris AG, Baden-Daettwil, Switzerland)

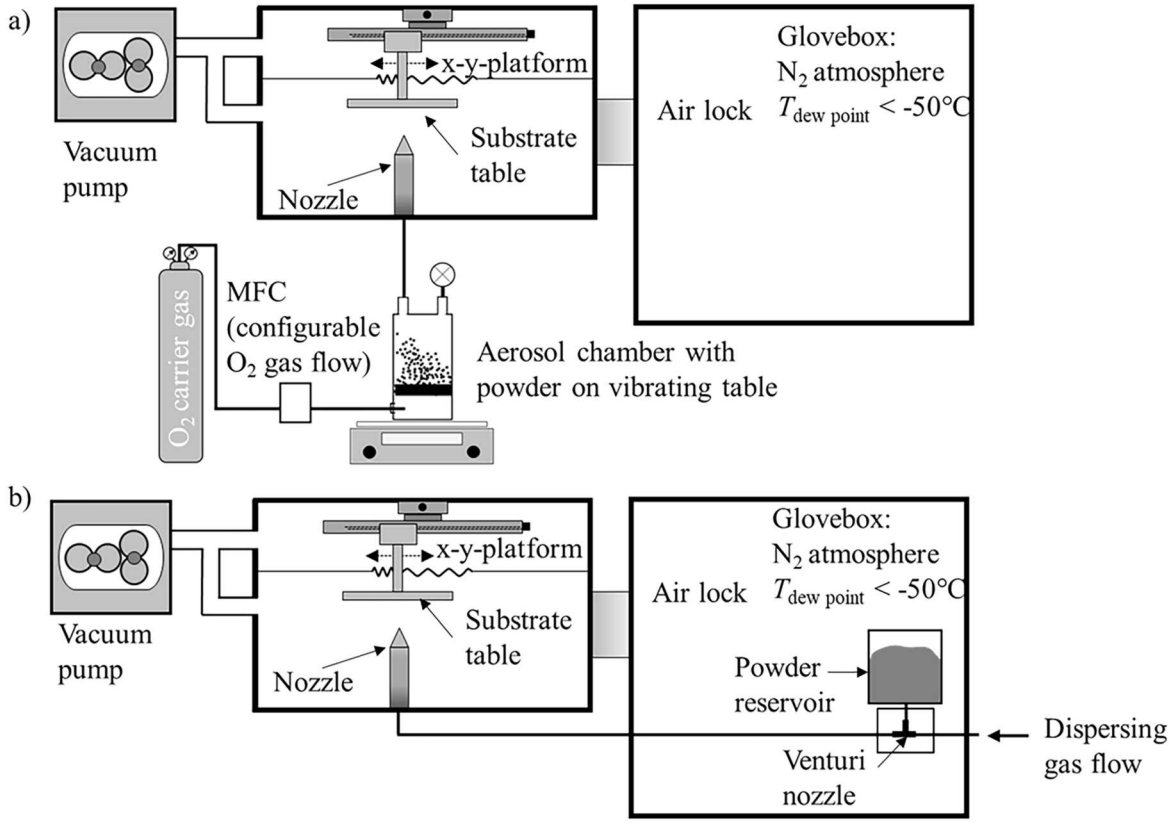

Figure 1. Schematic illustration of the used PAD apparatus for (a) cathode layer and (b) electrolyte layer fabrication. Adapted from.[13]

in a Bragg-Brentano arrangement. The samples were analyzed in the 2Θ range of 5° to 30°. For the powders, a point range of 0.015° for a hold time of 60 s and for the films the same point range with a hold time of 80 s was applied.

ICP-OES analysis.—9 different NMC/LLZO compositions were prepared with NMC contents from 10 wt-% (11 vol-%) to 90 wt-% (91 vol-%) with a 10 wt-% increase between each composition. For each composition, a powder sample and three PAD-films were prepared and characterized.

Prior to characterization by ICP-OES, the samples were dissolved via microwave-assisted acid digestion using an aqueous HNO_3/HCl solution (2 ml/6 ml). The digestion was performed in a Multiwave 3000 system (Anton Paar GmbH, Graz, Austria) at 1400 W (ramp rate 10 W min^{-1}) for 60 min, with a maximum pressure of 60 bar (ramp 0.5 bar s^{-1}) and a temperature of 240 °C.

Subsequently, an ICP-OES Optima 7300 DV (PerkinElmer, Connecticut, USA) equipped with an unbaffled cyclonic chamber nebulizer and a Meinhard nebulizer (Colorado, USA) was used to quantify the concentrations of lanthanum (La 379 nm) and nickel (Ni 221 nm). The obtained counts were then used to determine the compositions of the analyzed powders and films.

Focused ion beam milling and energy dispersive X-ray spectroscopy (EDS).—EDS was performed on FIB cross-sections of films used for cycling. Therefore, the films were removed from the PAT-Cells and the lithium was carefully removed from the film surface. The FIB cross-sections were prepared using a Helium-Ion-Microscope (NanoFab, Zeiss, Oberkochem, Germany) with a gallium-FIB column. For EDS measurements the samples were transferred to a scanning electron microscope (Merlin, Zeiss, Oberkochem, Germany) under argon using an air-thight transfer system (VCT 100, Leica Microsystems, Wetzlar Germany). The EDS measurements were conducted with an X-Max 80 detector (Oxford Instruments, Abingdon, UK) and an acceleration voltage of 20 kV.

Determination of the film thicknesses.—Film thicknesses of the samples used for electrochemical characterization were determined using a Mahr S2 Perthometer (Carl Mahr Holding GmbH, Göttingen, Germany). For each batch fabricated, an additional sample not used for electrochemical characterization was employed for thickness measurements, in order to prevent sample contact with humid air prior to other characterization methods. An overview of the measured film thicknesses of the fabricated PAD-SSBs used in the cycling experiments is displayed in the supporting information (Table S2, section S3).

Electrochemical characterization.—Galvanostatic cycling and electrochemical impedance spectroscopy (EIS) to characterize the fabricated PAD-SSBs were conducted with an Arbin LBTX20084 cell tester (Arbin Instruments, Texas, USA) in combination with a Gamry Interface 1010E (Gamry Instruments Inc., Pennsylvania, USA). Currents in the range of 1 μA to 4 μA were applied for cycling experiments, and the corresponding current densities were calculated based on the area of the lithium anode determined post-mortem. An overview of the determined lithium anode areas can be found in the supporting information in Table S2 in section S3. EIS during cycling experiments was conducted in potentiostatic mode with an amplitude of 25 mV within the frequency range of 1 MHz to 0.1 Hz with ten steps per decade. The EIS spectra were analyzed using the software Relaxis 3 (rhd instruments, Darmstadt, Germany).

To investigate the influence of thermal annealing on the resistance of PAD-NMC, EIS analyses in potentiostatic mode were performed in the range of 10 MHz to 1 Hz with an amplitude of 20 mV using a Novocontrol α-Analyzer (Novocontrol Technologies GmbH & Co. KG, Montabaur, Germany). The pure ohmic resistance was then extracted from the intersection of the spectrum with the real axis.

Results

Structural and compositional film characterization.—In order to characterize the film composition, XRD and ICP-OES analyses were carried out. XRD measurements were performed on the raw NMC and LLZO powders, as well as on the three cathode films used for cycling experiments: NMC, Composite A, and Composite B. The results are shown in Fig. 2a.

The diffraction patterns of the powders as well as the deposited films show reflections that indicate the desired layered oxide crystal structure for NMC and the desired garnet-type crystal structure characteristic for LLZO. The pattern of the PAD-NMC film reveals a distinct shift in intensity distribution in contrast to the NMC powder pattern. The (003) reflection becomes clearly pronounced, while the intensity of the other reflections is significantly reduced. This observation suggests a texture of the NMC film, indicating a preferential orientation of the crystallites with their *c*-axis perpendicular to the substrate plane. This finding is in line with results reported for other layered oxide materials deposited with PAD.[27,30,40–42] In addition, the reflections observed for PAD films are noticeably broadened compared to those of the initial powders. This broadening is attributed to the characteristic microstructure of PAD-deposited films. As a result of the deposition mechanism, the films exhibit a decreased crystallite size and an enhanced microstrain.[15,43]

The diffraction patterns of the PAD composite films show the desired reflections of both NMC and LLZO phases suggesting a

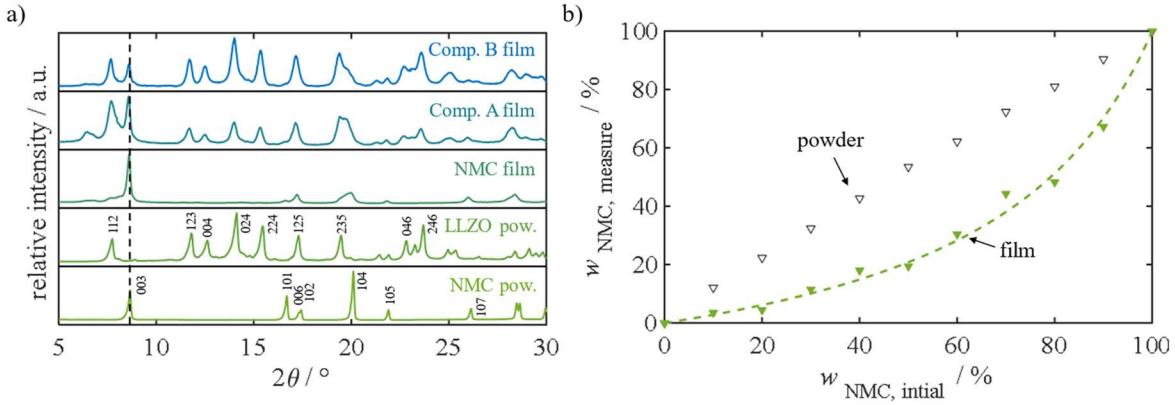

Figure 2. (a) XRD diffraction pattern of NMC powder, LLZO powder, PAD-NMC film, PAD-Composite A film, and a PAD-Composite B film, and (b) NMC weight content determined by ICP-OES relative to the initial powder composition for composite powders (black) and PAD-composite films (green). The green dashed line represents a fit of the obtained data for the determination of the composition after film fabrication. A detailed description of the fit is provided in section S1 in the supporting information.

successful co-deposition of Composite A and B. Reflection broadening is observed owing to already discussed decreased crystallite size and increased microstrain as result of the deposition mechanism.[15,43]

For quantitative analysis of the film compositions after film deposition, ICP-OES measurements were performed. To evaluate changes in composition during the film manufacturing process, the measured compositions of the as-deposited films were compared to that of the initial powders. For the quantitative analysis, lanthanum and nickel contents were determined and used to calculate the NMC content in the respective samples. The experimentally determined NMC weight content in the films ($w_{\mathrm{NMC,\ measure}}$) was correlated with the NMC weight content ($w_{\mathrm{NMC,\ initial}}$) that was weighed in. The results are shown in Fig. 2b.

The powder compositions (black triangles) remain consistent to the intended powder compositions used for the preparation of the composite powders. In contrast, the PAD films (green triangles) exhibit a reduced NMC weight content. This deviation could be attributed to two factors: First, the deposition rate of NMC may be lower than that of LLZO, resulting in preferential deposition of LLZO. Second, LLZO may have a more pronounced tendency for aerosol formation, leading to an increased LLZO concentration in the aerosol used for film fabrication.

The resulting film compositions were fitted (green dashed line) to enable a reliable determination of the compositions applied in the subsequent stages of this study. A detailed description of the fit is provided in section S1 in the supporting information. From the fit function (green dashed line), the NMC weight contents for the cycling experiments were derived as 38 wt-% (39 vol-%) for Composite A and 15 wt-% (15 vol-%) for Composite B.

To confirm successful cell fabrication of the multilayer films, EDS was performed on FIB cross-sections prepared from cells used for electrochemical characterization. The EDS measurements were conducted after the completion of the electrochemical tests. The results are shown in Fig. 3 for the PAD-SSB with a pure NMC cathode layer (cell 1) and in figure S1 and S2 in section S2 of the supporting information for the PAD-SSBs with a Composite A (cell 2) and Composite B (cell 3) cathode. For EDS-mapping nickel (blue) and lanthanum (green) were used representing the CAM and the SE, respectively. EDS mapping confirmed the desired cell architecture with a (composite) cathode layer and an electrolyte layer for all cells.

Cycling performance of PAD-SSB with a plain NMC cathode.—The results of the electrochemical characterization of the PAD-SSB with a pure NMC cathode layer (cell 1) are displayed in Fig. 4. Figures 4a and 4b show the charge-discharge curves, obtained capacities ($q_{\mathrm{dischr.}}$), and the coulombic efficiencies (η_{CE}) at different current densities. A specific capacity of 141 mAh g^{-1} is achieved at a current density of 5.0 μA cm^{-2} dropping to 92 mAh g^{-1} at a current density of 20.0 μA cm^{-2}. When the current density is reduced back to 5.0 μA cm^{-2}, the capacity partially recovers to 128 mAh g^{-1}. Over 25 cycles, a capacity retention of 90 % is obtained, while 69 % of the nominal capacity of 205 mAh g^{-1} (according to the data sheet provided by the manufacturer) can be utilized. The coulombic efficiency is determined to be 85 % for the first cycle and increases to > 97 % after the third cycle.

The EIS spectra shown in Figs. 4c and 4b consist of two slightly depressed semicircles in the high and mid frequency range with an increasing imaginary part of the impedance towards lower frequencies. A quantitative investigation of the data is performed using the commonly used method of equivalent circuit fitting. A model structure of RQ_1-RQ_2-Q_3 with two non-ideal resistive-capacitive elements (RQ) in series to a constant phase element (Q) seems appropriate. A detailed overview of the fit parameters is given in Table S3 in section S3 of the supporting information. The recorded spectra during cycling reveal an overall resistance increase (sum of R_1 and R_2) of approximately 42 % from the 1st to the 21st cycle, with the most pronounced change occurring between the 1st and 6th cycle. Notably, only the resistance associated with the RQ element in the mid-frequency range (R_2Q_2) increases throughout cycling. The variation of the SOC shown in Fig. 4d does not exhibit any significant influence on the overall impedance. The various SOCs were determined and approached based on the time elapsed during the initial cycle. The EIS spectra remain largely unchanged across different SOC of 0%, 50% and 100%. The various SOCs for this and for the following experiments were determined and approached based on the time elapsed during the initial cycle.

Cycling performance of PAD-SSB with composite cathodes.—To investigate the effect of LLZO as catholyte in the cathode, PAD-SSBs with a Composite A (cell 2) and a Composite B (cell 3) cathode layer were electrochemically characterized. An overview of the data for cell 2 is shown in Fig. 5. Charge-discharge curves as well as EIS spectra to investigate the effect of the SOC are shown in the supporting information (Fig. S3, section S3). At a current density of 6.3 μA cm^{-2}, a capacity of 86 mAh g^{-1} is achieved, which decreases to 39 mAh g^{-1} at 25.0 μA cm^{-2}. When the current density is reduced back to 6.3 μA cm^{-2}, capacities of 79 mAh g^{-1} can be obtained corresponding to a capacity retention of 91 % over 25 cycles. This accounts for 42 % of the nominal capacity. The coulombic efficiency for the first cycle is 33 % and increases to values between 80 % and 90 % after the fifth cycle.

The EIS spectra in Fig. 5b exhibit a similar trend to that observed for cell 1. Once more, two slightly depressed semicircles can be observed with the imaginary part of the impedance increasing towards lower frequencies. A quantitative analysis of the data was carried out with a model structure of RQ_1-RQ_2-Q_3. A detailed overview of the fit parameters is given in Table S4 in section S3 of the supporting information. The overall resistance increases by 45%

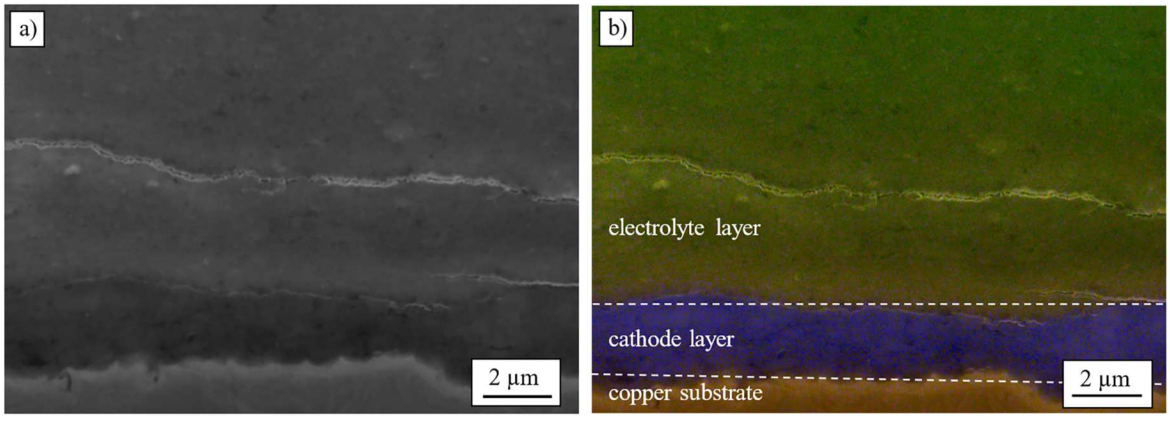

Figure 3. (a) SEM image of a FIB cross-section of cell 1 with an NMC cathode layer. (b) EDS mapping showing the distribution of copper (orange), nickel (blue), and lanthanum (green), representing the substrate, the CAM, and the SE, respectively.

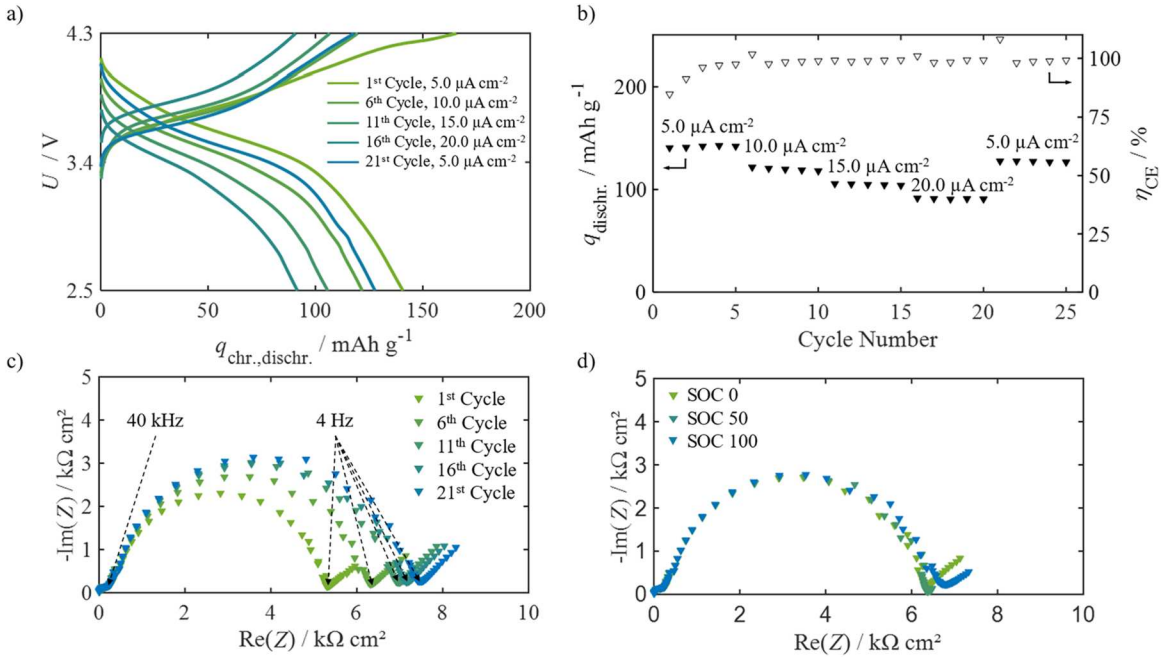

Figure 4. Electrochemical characterization of a PAD-SSB with a PAD-NMC cathode layer ($d \sim 1.5$ µm) and a PAD-LLZO electrolyte layer ($d \sim 26$ µm) in the as-deposited state (cell 1). (a) Charge-discharge curves at different current densities. (b) Discharge capacities and coulombic efficiencies obtained during cycling. (c) Selection of EIS spectra recorded during cycling (SOC = 0%) and (d) EIS spectra of the cell at different SOCs. All experiments were conducted at 70 °C with an applied external pressure of ~3 MPa.

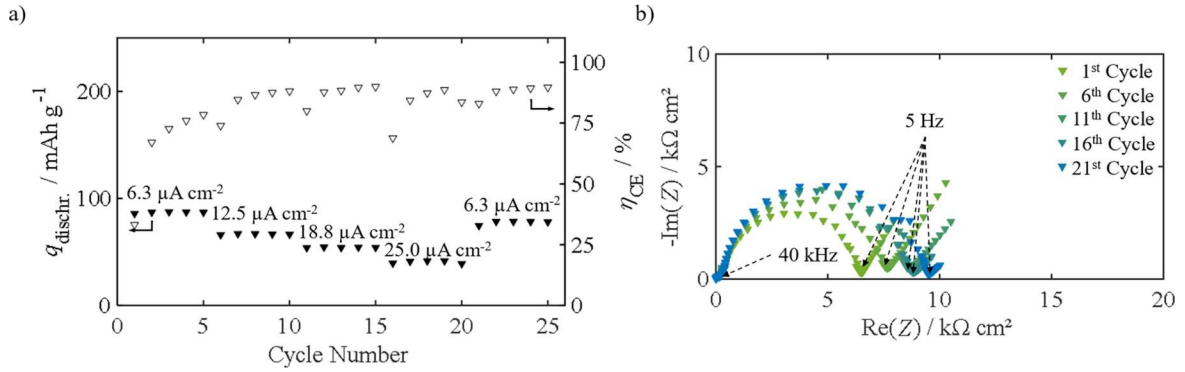

Figure 5. Electrochemical characterization of a PAD-SSB with a PAD-Composite A cathode layer ($d \sim 0.9$ µm) and a PAD-LLZO electrolyte layer ($d \sim 26$ µm) in the as-deposited state (cell 2). (a) Discharge capacities and coulombic efficiencies obtained during cycling. (b) selection of EIS spectra recorded during cycling (SOC = 0%). All experiments were conducted at 70 °C with an applied external pressure of ~3 MPa.

from the 1st to the 21st cycle with the most significant increase taking place between the 1st and 6th cycle. Again, the increase in resistance throughout cycling only affects the *RQ* element in the mid-frequency range (R_2Q_2). EIS analyses across varying SOC show no notable differences in the overall cell impedance (cf Fig. S3b, section S3 in the supporting information).

A selection of the data retrieved for the electrochemical characterization for cell 3 is displayed in Fig. 6, while additional data can be found in Fig. S4 in section S3 in the supporting information. At a current density of 4.2 µA cm^{-2}, a capacity of 76 mAh g^{-1} can be obtained. Increasing the current density to 16.7 µA cm^{-2} results in a capacity of 46 mAh g^{-1}, which increases back to 70 mAh g^{-1} after decreasing the current density back to 4.2 µA cm^{-2}. This equals a capacity retention of 89 % over 25 cycles and a utilization of 37 % of the nominal capacity. A coulombic efficiency of only 28 % is determined for the 1st cycle, but it increases to values between 85 % and 96 % after the fifth cycle.

The EIS spectra displayed in Fig. 6b were analyzed according to the procedure conducted for cell 1 and cell 2. Again, the spectra consist of two slightly depressed semicircles with an increasing imaginary part at low frequency. Quantitative analyses were performed with a model structure of RQ_1-RQ_2-Q_3. The results show an increase in resistance of approximately 80 % from the 1st to the 21st cycle, with the most pronounced change occurring once more between the 1st and 6th cycle. Only the resistance associated with the *RQ* element in the mid-frequency range is affected throughout cycling. Again, the variation of the SOC (cf Fig. S6b, supporting information section S4) has no effect on the ohmic resistance of the cell. The various SOCs were determined and approached based on the time elapsed during the initial cycle.

Overview on cycling properties and effect of thermal annealing.—The capacities of cell 1 to cell 3 are summarized in Fig. 7a, showing the determined capacities of the 1st and 21st cycle (green triangles) as function of the cathode composition. The highest capacity is achieved for cell 1, reaching 67 % of the nominal capacity of 205 mAh g^{-1}. An increase in LLZO weight content within the cathode layer results in reduced utilization of the cathode active material. Despite these differences in initial capacity, the capacity retention across all cells remains largely comparable at around 90 %.

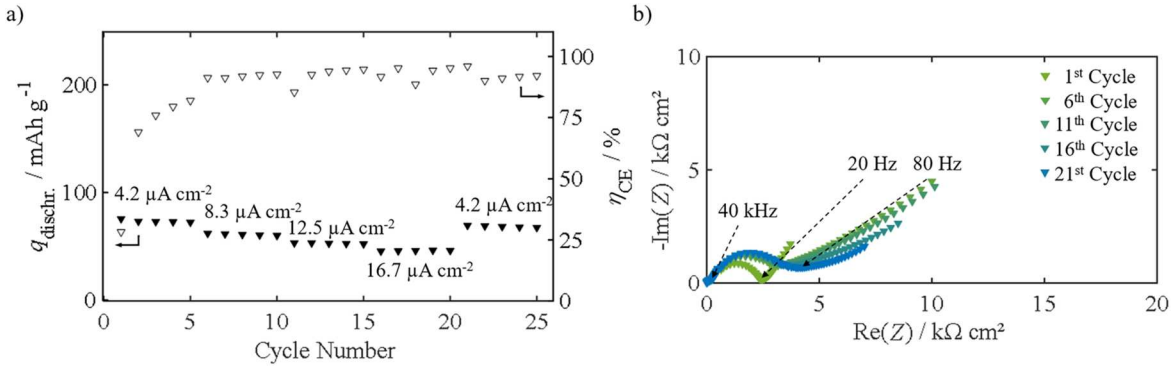

Figure 6. Electrochemical characterization of a PAD-SSB with a PAD-Composite B cathode layer ($d \sim 1.5$ µm) and a PAD-LLZO electrolyte layer ($d \sim 22$ µm) in the as-deposited state (cell 3). (a) Discharge capacities and coulombic efficiencies obtained during cycling. (b) selection of EIS spectra recorded during cycling (SOC = 0%). All experiments were conducted at 70 °C with an applied external pressure of ~3 MPa.

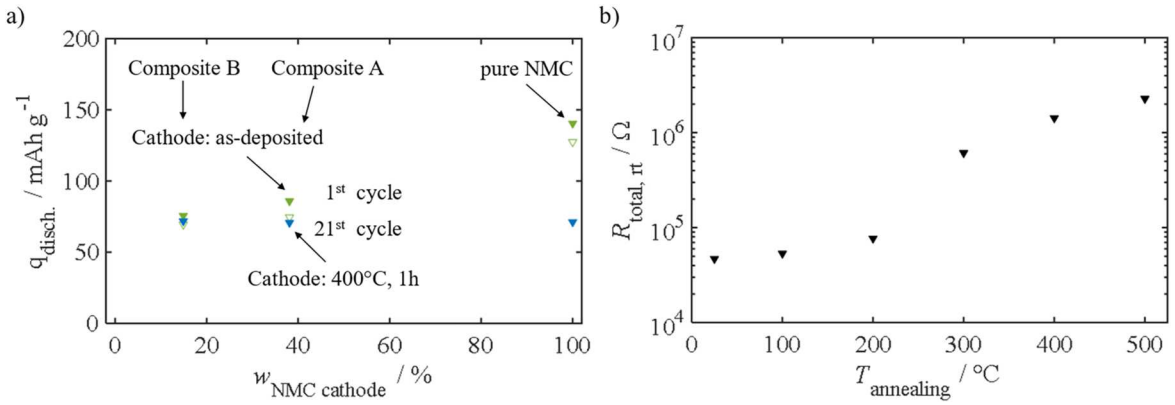

Figure 7. (a) Overview of the measured capacity for PAD-SSBs with cathodes layers (green) in the as-deposited state and cathode layers annealed at 400 °C for 1 h (blue) with respect to the NMC weight content ($w_{NMC\ cathode}$). The electrolyte layer of the investigated cells remained in the as-deposited state. (b) Resistance of an NMC film with respect to the annealing temperature determined by EIS analysis at room temperature.

It is well known that microstrain, resulting from the characteristic deposition mechanism of the PAD process, negatively affects the electrochemical properties of the films. Microstrain correlates with reflex broadening observed in XRD and originates from variations of the lattice parameter, i.e., from local strains and stresses including gradients. The high strains alter electronic and ionic properties and lead to reduced conductivities compared to the corresponding unstrained bulk material. Microstrain in the films can be reduced by thermal annealing at mild temperatures well below the melting point or sintering temperature.[16,17,43,44] To investigate the impact of thermal annealing on the capacity of PAD-SSBs, cycling experiments were performed with cells that include cathode layers that were annealed for 1 h, while the electrolyte layer remains in the as-deposited state since it was deposited after annealing. In terms of annealing temperature, Hanft et al. identified 400 °C as being optimal for reducing microstrain in LLZO films.[21] Since LLZO is used as an additive in the composite cathodes investigated in this study, the same annealing temperature was applied. As in previous experiments, PAD-SSBs including pure NMC (cell 4), Composite A (cell 5) as well as Composite B (cell 6) cathode layers were investigated. A detailed overview of the collected data on the cells with annealed electrodes is given in Figs. S5 to S7 (section S4 in the supporting information) and the determined capacity of the 1st cycle as function of the cathode composition is displayed in Fig. 7a (blue triangles).

The capacity during the first cycle of the PAD-SSB with an annealed NMC cathode layer (cell 4) decreases from 141 mAh g^{-1} in the as-deposited state to 71 mAh g^{-1} in the annealed state. A similar trend can be observed for the PAD-SSB with a Composite A cathode layer (cell 5), where the capacity decreases from 86 mAh g^{-1} in the as-deposited state to 71 mAh g^{-1} in the annealed state. The PAD-SSB with a Composite B cathode layer (cell 6) maintains its capacity and seems not affected by the annealing process.

It is well known that annealing can release microstrain and that microstrain negatively affects the mobility of charge carriers. Consequently, annealing usually leads to improved electrochemical properties. A phenomenon, that has been already demonstrated across various material systems, especially for LLZO.[21,35,45–47] However, the observations made in this study contradict this literature findings.

To further investigate the effect of annealing on the electrochemical properties of a PAD-NMC film, EIS spectra of PAD-NMC films after annealing at different temperatures were taken. The results are displayed in Fig. 7b, showing the ohmic resistances ($R_{total,\ rt}$) as function of the annealing temperature. EIS analyses were conducted at room temperature after each annealing step. The resulting EIS spectra are shown in Fig. S8a (section S5, supporting information).

The resistance gradually increases up to 200 °C. Between 200 °C and 300 °C, the resistance increases by one order of magnitude, followed by a continued gradual increase up to 500 °C. Beyond 500 °C, no meaningful EIS spectra can be obtained after annealing at 600 °C and 700 °C. Inspection of the PAD-NMC film post-annealing (Fig. S8b, section S5, supporting information) reveals that platinum from the contacting 4-wire structure has diffused through the film onto its surface. A similar experiment using a PAD-NMC film deposited on Al_2O_3 with a copper 4-wire structure yielded comparable results (cf Fig. S9 section S5, supporting information). As already observed for platinum, copper appears to diffuse through the film during annealing.

Table I. Overview on data reported in literature on PAD-SSBs and PAD-cathode layers in comparison to the data achieved in this study.

Cathode layer		$d_{cathode}$/μm	Electrolyte layer		$q_{dischr.}$/mAh g^{-1}	j/μA cm^{-2}	T/°C	References
LFP	PAD	1	LLZO	PAD	53	5	140	37
NMC/LATP	PAD	20	LLZO	bulk	135	50	100	25
LCO	PAD	1	LGVO LLZO	PAD bulk	83	2.9	60	31
LCO/LBO	PAD	5.6	LLZO	bulk	128	30	60	28
LCO/LATP	PAD	15	LLZO	bulk	130	50	100	32
cell 1	PAD	1.5	LLZO	PAD	141	5	70	this work
cell 2	PAD	0.9	LLZO	PAD	110	6.3	70	this work
cell 3	PAD	1.5	LLZO	PAD	73	4.2	70	this work

Discussion

Benchmarking against the current state of the art.—The aim of this study was to give an overview of the current progression of the cycling performance in terms of capacity and impedance behavior for PAD-SSBs. For only the second time, it was demonstrated that SSBs with a cathode and electrolyte layer fabricated via PAD can be cycled over multiple cycles without cell failure. Capacities of up to 141 mAh g^{-1} – 67 % of the nominal capacity of the utilized CAM — with high capacity retentions of 90 % over 25 cycles were achieved using NMC as CAM.

The only other PAD-SSB cycled over multiple cycles was reported by Ahn et al.[39] They utilized a PAD-SSB consisting of an LFP cathode layer and an LLZO electrolyte layer achieving capacities of 53 mAh g^{-1} — which is 33 % of the nominal capacity of the utilized CAM. The capacity drastically decreased by almost 75 % in the second cycle at a current density of 5 μA cm^{-2} at 140 °C.

Apart from that, comparable studies were usually conducted with PAD cathode films deposited on electrolyte pellets to form SSBs. Kato et al. utilized an NMC/$Li_{1+x}Al_xTi_{2-x}(PO_4)_3$ (LATP) composite deposited on an LLZO pellet. At 50 μA cm^{-2} and 100 °C, a capacity of 135 mAh g^{-1} (75 % of the nominal capacity) was achieved, while the cell could be cycled over 90 cycles, maintaining a capacity retention of 97%.[28] Sakakura et al. prepared a PAD-LCO cathode layer on an LLZO substrate equipped with a PAD deposited LISICON-type $Li_{3.5}Ge_{0.5}V_{0.5}O_4$ (LGVO) interlayer. After annealing at 700 °C, they achieved a capacity of approximately 40 μAh cm^{-2} which corresponds to 83 mAh g^{-1} (55 % of the nominal capacity) — assuming a film density of 95 % — at a current density of 2.9 μA cm^{-2} and 60 °C.[34] Cheng et al. used LCO precoated with Li_3BO_3 to form PAD films on a LLZO pellet. At a current density of 30 μA cm^{-2} and a temperature of 60 °C, a specific capacity of 128 mAh g^{-1} (85 % of the nominal capacity) was achieved. Over 30 cycles, a capacity retention of 84 % with coulombic efficiencies of approximately 99 % was reported.[31] Finally, Sakakura et al. utilized LCO/LATP composites on LLZO pellets, achieving 130 mAh g^{-1} (87 % of the nominal capacity) at a current density of 50 μA cm^{-2} and a temperature of 100 °C.[35] The literature results are summarized and compared in Table I.

Even though complete comparability is not always possible due to differences in measurement temperature, applied current densities or cell design in terms of cathode film thickness and cathode composition, the data presented here demonstrate a substantial progress in cycling performance for SSBs with both PAD-cathode and -electrolyte layer. The capacities achieved match — and in some cases even surpass — those reported in previous studies employing PAD-fabricated cathodes in combination with bulk electrolyte architectures, underscoring the potential of PAD-SSBs.

Challenges for PAD-SSBs.—Despite the progress made by the results presented, several key challenges remain to be addressed. These challenges can be divided into two categories, improvements with respect to the electrolyte layers and to cathode layers. While previous studies have demonstrated that thermal annealing can improve the ionic conductivity and reduce the resistance of PAD-LLZO films,[11,21] the focus of this work lies on strategies to enhance the cathode layers and their performance — specifically aiming to achieve higher capacities for improved energy densities. For a broader context on PAD electrolyte films the studies of Hanft et al., Nazarenus et al. and Hennerici et al. are referred to.[11,13,21]

Based on the findings of this study, three main challenges need to be addressed:

I. Film thickness of cathode films for high energy densities
II. Suitability of nickel-rich NMC as CAM for PAD-SSBs
III. Interaction of nickel-rich NMC and LLZO as composite for the cathode layer

The following section discusses these challenges in detail with respect to the specific results obtained from the experiments conducted in this study.

It should be noted that further in-depth evaluation of the EIS data will not be considered. The characteristic microstructure — particularly the grain sizes in the 10 nm range and the presence of microstrain — has a significant influence on the impedance. The precise effects of this characteristic on the impedance have not yet been investigated in literature. Therefore, the individual systems should first be examined in isolation. Building on these findings, an evaluation of a multilayer system containing material mixtures as a composite, as investigated in the present study, would then be feasible. However, this would go beyond the scope of the current work.

Film thickness of cathode films for high energy densities.—In this study, cathode film thicknesses of around 1 μm were utilized. However, a cathode layer thickness in this range is not sufficient to meet the requirements for high capacities and high energy densities. To surpass the energy densities achieved by conventional LIB, target values of at least 800 Wh L^{-1} and 300 Wh kg^{-1} must be reached.[1,13] To fully exploit the potential of SSBs and particularly lithium metal as anode active material even higher values for energy densities are required.

Suitability of NMC as CAM.—While thicker cathode layers could in theory lead to higher energy densities, the utilization of thicker PAD-NMC films leads to a significant reduction in specific capacity, resulting in lower energy densities. As reported previously, utilizing a PAD-SSB with a cathode layer based on NMC as CAM with film thickness of 25 μm only a capacity of 7 mAh g^{-1} at a current density of 13 μm cm^{-2} can be obtained.[13] This may lead to the assumption that, regardless of cathode thickness and the resulting CAM loading, only a portion of the capacity of the active material can be utilized. It is conceivable that, at higher thicknesses, only the regions of the cathode layer close to the electrolyte layer participate in the charge–discharge process, while the areas near the current collector remain inactive.

This observation and hypothesis may be attributed to two phenomena, namely microstrain and the texture of the electrode. First, the reduction of microstrain introduced during the deposition of PAD-NMC films must be considered. As previously discussed, such microstrain negatively impacts the film's conductive properties and low-temperature annealing can be employed to mitigate these effects. However, as shown in Fig. 7b, annealing PAD-NMC films yields results contrary to expectations: instead of reducing resistance and thereby enhancing conductivity, the overall resistance increases with rising annealing temperature.

It is known that NMC ($LiNi_{1-x-y}Mn_xCo_yO_2$) is thermally unstable in its delithiated state, with the onset temperature for decomposition decreasing as the nickel content increases.[48,49] While fully lithiated NMC is assumed to exhibit higher thermal stability compared to its delithiated counterpart, the experimental results suggest that metal from the screen-printed four-wire structures may diffuse through the films at elevated temperatures as indicated by the changes observed after annealing (cf Figs. S8b and S9b, section S5 supporting information). This suggests a certain thermal instability of fully lithiated NMC in contact with Pt and Cu. To date, no literature has reported decomposition reactions of nickel-rich NMC in direct contact with Pt or Cu as well as for other metal materials used for contacting of the cathode layer. Consequently, any assumptions regarding the exact processes occurring at elevated temperatures would be premature without further investigation.

Besides microstrain, a second phenomenon that negatively influences the cycling properties of PAD-NMC films may be the texture observed during XRD analysis, as shown in Fig. 2a. This preferential orientation results in the (003)-plane alignment parallel to the current collector. In the layered oxide crystal structure of NMC, described by the *R*–3*m* space group, the (003)-plane corresponds to the stacking of oxide layers, in which lithium and transition metal ions (nickel, manganese, cobalt) occupy distinct and alternating octahedral layers. Lithium resides in one layer, while the transition metal ions occupy the other layer, resulting in a well-defined layered structure.[50]

A consequence of this crystal structure is that lithium-ion diffusion is largely confined to two dimensions, parallel to the oxide layers, due to the ion blocking nature of the transition metal layers.[51] With respect to the preferential orientation observed in PAD-NMC films, the alignment of the ion blocking layer parallel to the current collector may impede lithium ion transport through the cathode layer toward the electrolyte layer and may be problematic, particularly for thicker films.

After all, the phenomena under discussion provide a satisfactory explanation for the data obtained, particularly considering the findings that have been previously published. However, the hypotheses are based on data reported in literature. Further investigation would be required for validation, which would go beyond the scope of this work.

Interaction of nickel-rich NMC and LLZO as composite for cathodes.—Introducing the LLZO as SE into the cathode layer did not yield the intended effect. Instead of increasing the capacity through enhancing ionic conductivity, the capacity decreased from 141 mAh g^{-1} for the NMC cathode to 86 mAh g^{-1} for the Composite A cathode (38 wt-% (39 vol-%) NMC; 62 wt-% (61 vol-%) LLZO) and to 75 mAh g^{-1} for the Composite B (15 wt-% (15 vol-%) NMC; 85 wt-% (85 vol-%) LLZO) cathode. However, for cell 3 with Composite B, it should be noted that the low amount of CAM may also result in poor connectivity of CAM particles. Potentially, this could lead to electronically inactive CAM particles, as suggested by simulations from Clausnitzer et al.[17] Furthermore, the addition of LLZO to the cathode leads to a significant decrease in the coulombic efficiency from cell 1 to cell 2. A partial recovery is observed from cell 2 to cell 3, although the efficiency does not reach the values achieved for cell 1.

In addition, the EIS spectra measured with respect to varying SOC do not indicate any effect of the solid electrolyte addition to the cathode. It is evident that the impedance response is not dominated by the cathode layer and that a single process governs the impedance behavior across all SOCs. Since the typical influence of the SOC on the impedance of a battery is not present, it can be assumed that the process is most likely related to a contribution of the electrolyte layer like electrode/electrolyte interface or grain boundary effects.

Generally, simulations by Clausnitzer et al. show that high CAM fractions (> 70 vol-%) would lead to a significant drop in capacity due to increased ionic tortuosity and decreased connectivity of the CAM to the SE phase.[19] Especially at low SOC, the addition of LLZO is meant to compensate for the decreased lithium ion diffusivity in the CAM.[52] Literature on the subject is scarce when it comes to experimental data on LLZO/NMC composites with the specific composition used in this study and LLZO/CAM composites in general.[8] Existing studies typically do not include a direct comparison of the cycling performance of cathodes with and without a solid electrolyte additive as catholyte.[53–55]

This raises the question of what impedes the electrochemical performance in the composite cathode layers. Once again, a possible factor contributing to the reduced capacity may be the microstrain in as-deposited PAD films. It is conceivable that PAD-LLZO films are more susceptible to this microstrain-induced degradation of the conductive properties than PAD-NMC films. As a result, the addition of LLZO to the composite cathode may impair charge carrier transport rather than enhance it.

A second possible factor may be the interaction between LLZO and NMC during cycling. As indicated by the decrease in coulombic efficiency from cell 1 to cell 2 (> 97 % vs 80 % – 90 %) and the overall lower efficiency during the initial cycles, the increased LLZO weight content — and the resulting larger interfacial area between NMC and LLZO particles — appears to promote unwanted side reactions. These side reactions may also be responsible for the substantial increase in cell impedance observed across all cells characterized in this study.

Similar observations and assumptions were reported in the literature with respect to the observation made during the initial cycles.[8,54–56] These observations were attributed to the electrochemical instability of LLZO in the presence of CAMs. Especially at higher SOC, interphase formation as a result of cation diffusion between LLZO and CAM may result in the formation of interfacial layers with higher resistances, as shown by Ihrig et al. using LLZO and LCO.[56]

However, the behavior of the cells investigated in this study differs from previously reported data on LLZO/LCO composites beyond the initial cycles. While literature reports significantly higher coulombic efficiencies after the initial cycles, substantial capacity fading is observed.[53–56] This behavior is typically associated with mechanical degradation, such as volume changes during delithiation of the CAM, which can lead to contact loss between CAM and LLZO within the cathode layer beyond the initial cycles.[8] Although volume changes may contribute to the observed trends, the results presented in this study are more likely linked to the continued formation of an insulating interphase beyond the initial cycles as indicated by the low coulombic efficiency. This phenomenon is presumably driven by the electrochemical instability of both LLZO and the nickel-rich NMC employed. It should be emphasized that the discussed hypotheses are based on data reported in literature. Further characterization is needed to validate the hypotheses. However, such investigations would go beyond the scope of this work.

Outlook and Perspective

Following the identification of challenges based on the findings of this study, the subsequent section will present a range of strategies to address these challenges. The individual strategies to overcome each of the three challenges discussed in the previous sections are discussed separately.

Film thickness of cathode films for high energy densities.—In an effort to determine suitable cathode layer thicknesses for

achieving higher energy densities, we recently demonstrated that such energy densities require cathode layers of at least 50 μm.[14] Building on this prerequisite, we aimed to maximize the thickness of PAD-NMC films. By employing a step-like film architecture, we showed that PAD-NMC films with thicknesses of at least 145 μm can be fabricated simply by increasing the deposition duration. Notably, no saturation in film growth was observed, suggesting that even higher thicknesses can be achieved.[13] Consequently, the film thickness can already be readily adapted to meet specific energy density demands using PAD as fabrication method.

Suitability of NMC as CAM.—Thermal instability and the textured microstructure of PAD-NMC films were identified as a possible challenge for NMC as CAM. A possible strategy to mitigate such thermal instability or decomposition in contact with metallic materials could be to reduce the nickel content in NMC (e.g. to $LiNi_{0.6}Mn_{0.2}Co_{0.2}O_2$). Although thermal stability is primarily studied in the delithiated state, lower nickel contents may also improve the stability in the lithiated state. Another strategy involves optothermal post-treatment, in which PAD films are exposed to radiation emitted by high-power LEDs.[57] This method may allow for lower temperatures and shorter durations compared to conventional thermal annealing, thereby limiting decomposition—ideally avoiding it entirely. Especially, the significantly shorter annealing durations of only a few seconds could be beneficial for this purpose.

Additionally, alternative experimental setups could be employed to investigate the effect of thermal annealing on PAD-NMC films while avoiding direct contact with metallic materials. For instance, PAD-NMC films could be deposited onto bulk electrolyte samples. Thereby, the contacting of the cathode layer with metallic materials could be performed after the annealing step preventing contact at elevated temperatures.

In terms of the textured microstructure of PAD-NMC films, up to now, no investigations have been conducted to analyze the impact of texture on the anisotropic conductivity of PAD-NMC electrodes, specifically comparing in-plane and through-plane conductivity. Further efforts could therefore be devoted to studying the effects of this anisotropy. It should be examined whether such anisotropy could hinder ionic charge transport, thereby limiting the application CAM with layered crystal structure, i.e. NMC or LCO, for high-energy-density PAD-SSBs.

Interaction of nickel-rich NMC and LLZO as composite for cathodes.—As indicated by the lower coulombic the electrochemical instability of LLZO in contact with NMC was identified as a potential challenge. To address this challenge, further work should investigate the effect of a reduced area between LLZO and NMC as CAM.

A frequently used strategy to do so involves coated CAMs particles. However, Linz et al. demonstrated that during PAD deposition, the initial particle architecture is not maintained throughout the deposition, as only a small portion of each particle shell is incorporated into the film.[29] Consequently, CAM particles would no longer be fully covered by the original protective layer in the as-deposited PAD film.

A more suitable approach for PAD films could therefore involve replacing LLZO as catholyte with a material that exhibits greater electrochemical stability in contact with CAMs. Additionally, introducing a thin interlayer (~1 μm) between the cathode and LLZO electrolyte layer, composed of the replacement material, could further reduce direct contact between the CAM and LLZO. This would preserve the advantages of LLZO as an electrolyte layer, particularly its stability against lithium and its mechanical robustness against dendrite growth, while avoiding electrochemical degradation. A suitable candidate replacing LLZO could be the NASCION-like LATP. As already mentioned, Kato et al. reported the fabrication of a PAD-NMC/LATP composite film on a LLZO substrate showing a high capacity with a cathode layers thickness of 20 μm and an excellent capacity retention of 97 % over 90 cycles.[28]

Building on that, the influence of thermal annealing on composite PAD-cathodes should be investigated. PAD-LLZO films have been shown to benefit from thermal annealing, with conductivity increases of one to two orders of magnitude reported after treatment at 400 °C, likely due to microstrain relaxation.[11,21] In order to carry out such a study, the experimental setup should be adjusted in two key aspects. First, the PAD-LLZO electrolyte layer should be replaced with a bulk solid electrolyte. The use of PAD-electrolyte films introduces additional complexity and need of optimization to the system, as indicated by the different EIS analysis performed with respect to the SOC. Second, an NMC composition with a reduced amount of Ni may be more suitable for such investigations, as previously discussed.

Conclusions

In this study, we investigated the capacity of PAD-SSBs with nickel-rich NMC as CAM and LLZO as solid electrolyte and catholyte. A capacity of 141 mAh g^{-1} with a retention of 90 % over 25 cycles at 70 °C for a pure NMC cathode was achieved — a performance that has not been previously reported for PAD-SSBs in the literature. Notably, to this point no thermal post-treatment was applied after the film fabrication. Adding LLZO as catholyte for the fabrication of composite cathode layers led to an unexpected drop in capacity accompanied by an overall lower coulombic efficiency throughout cycling. Finally, the effect of a thermal annealing at 400 °C was investigated. It was demonstrated that the thermal annealing of the cathode layers resulted in reduced capacities during cycling. Further investigations of the effect of thermal annealing on the resistance of PAD-NMC films suggests a thermal instability of nickel-rich NMC in contact with pure metals. In light of these findings, remaining challenges for PAD-SSBs with the goal of maximizing energy density were identified and potential strategies for cathode layer optimization were discussed. To enhance capacity and cycle life of PAD-SSBs, potential strategies could involve (i) the reduction of the nickel content of NMC to enable thermal annealing to reduce microstrain and (ii) the utilization of an alternative catholytes as replacement for LLZO.

Acknowledgments

The authors would like to thank the German Federal Ministry of Education and Research (BMBF) within the framework of the FestBatt2 cluster (BMBF grant 03XP0441A and 03XP0441C) and the Bavarian Center for Battery Technology (BayBatt) for funding this research work. Support of the BayBatt Cell Technology Center is gratefully acknowledged, funded by the Deutsche Forschungsgemeinschaft (DFG, German Research Foundation)—INST 91/452–1 LAGG. The authors gratefully acknowledge the contribution of P. Hawe for the acquisition of the XRD data and C. Roth (Department of Electrochemical Process Engineering, University of Bayreuth) for providing the STOE STADI MP diffractometer. The instrument is funded by the Deutsche Forschungsgemeinschaft (DFG, German Research Foundation) - Project number 549313731. Furthermore, the authors would like to thank B. Brunner for performing the ICP-OES and A. Jess (Chair of Chemical Engineering, University of Bayreuth) for providing the ICP-OES equipment. The authors thank T. Wöhrl for the fabrication of Al_2O_3 substrates equipped with screen-printed platinum and copper 4-wire structures.

Author Contributions

Conceptualization, L.H., Methodology L.H. and R.M., Data Evaluation L.H., Film Fabrication L.H., D.B. and P.F., Film characterization L.H., and S.L., Electrochemical Characterization L.H., M.S. and P.F, Writing—Original Draft, L.H., Review & Editing L.H. and R.M., Supervision, D.K., R.Moe., M.A.D and R.M.

Declaration of Interests

The authors declare no competing interests.

ORCID

Lukas Hennerici https://orcid.org/0000-0002-1388-7662
Dominik Bröse https://orcid.org/0009-0008-8074-8196
Maximilian Schamel https://orcid.org/0000-0001-7527-3466
Sabrina Lang https://orcid.org/0009-0001-0450-1529
Paula Ficht https://orcid.org/0009-0003-0553-8600
Dominik Kramer https://orcid.org/0000-0002-9761-0627
Reiner Mönig https://orcid.org/0000-0003-1048-9973
Michael A. Danzer https://orcid.org/0000-0002-4135-7263
Ralf Moos https://orcid.org/0000-0001-7622-0120

References

1. J. Janek and W. G. Zeier, *Nat. Energy*, **1**, 16141 (2016).
2. A. Manthiram, X. Yu, and S. Wang, *Nat. Rev. Mater.*, **2**, 16103 (2017).
3. Z. Wu, Z. Xie, A. Yoshida, Z. Wang, X. Hao, A. Abudula, and G. Guan, *Renew. Sust. Energ.*, **109**, 367 (2019).
4. T. Ye, L. Li, and Y. Zhang, *Adv. Funct. Mater.*, **30**, 2000077 (2020).
5. Y. Wang, Z. Chen, K. Jiang, Z. Shen, S. Passerini, and M. Chen, *Small*, **20**, e2402035 (2024).
6. X. Shen, Q. Zhang, T. Ning, T. Liu, Y. Luo, X. He, Z. Luo, and A. Lu, *Mater. Today Chem.*, **18**, 100368 (2020).
7. Q. Liu, Z. Geng, C. Han, Y. Fu, S. Li, Y. He, F. Kang, and B. Li, *J. Power Source*, **389**, 120 (2018).
8. Y. Ren et al., *Adv. Energy Mater.*, **13**, 2201939 (2023).
9. E. Kurian, J. Pitchai, S. Neelanarayanan, and K. Ramesha, *RSC Appl. Interfaces*, **1**, 868 (2024).
10. Y. Zhao, L. Chen, Y. Su, H. Jin, and C. Wang, *J. Mater. Sci.*, **60**, 629 (2025).
11. T. Nazarenus, Y. Sun, J. Exner, J. Kita, and R. Moos, *Energy Technol.*, **9**, 2100211 (2021).
12. J. Schnell, T. Günther, T. Knoche, C. Vieider, L. Köhler, A. Just, M. Keller, S. Passerini, and G. Reinhart, *J. Power Source*, **382**, 160 (2018).
13. L. Hennerici, P. Ficht, M. Schamel, U. Mansfeld, M. Linz, D. Paulus, J. Kita, M. A. Danzer, and R. Moos, *Adv. Mater. Technol.*, **10**, 2400745 (2024).
14. J. Akedo, M. Ichiki, K. Kikuchi, and R. Maeda, *Sens. Actuators A: Phys.*, **69**, 106 (1998).
15. D. Hanft, J. Exner, M. Schubert, T. Stöcker, P. Fuierer, and R. Moos, *J. Ceram Sci. Technol.*, **6**, 147 (2015).
16. J. Akedo, *J. Am. Ceram. Soc.*, **89**, 1834 (2006).
17. J. Akedo, *J. Ceram. Soc. Japan*, **128**, 101 (2020).
18. S. Y. Kim, H. Cha, R. Kostecki, and G. Chen, *ACS Energy Lett.*, **8**, 521 (2023).
19. M. Clausnitzer, R. Mücke, F. Al-Jaljouli, S. Hein, M. Finsterbusch, T. Danner, D. Fattakhova-Rohlfing, O. Guillon, and A. Latz, *Batter. Supercaps*, **6**, e202300167 (2023).
20. P. Minnmann et al., *Adv. Energy Mater.*, **12**, 2201425 (2022).
21. D. Hanft, J. Exner, and R. Moos, *J. Power Source*, **361**, 61 (2017).
22. R. Inada, T. Okada, A. Bando, T. Tojo, and Y. Sakurai, *Prog. Nat. Sci.-Mater.*, **27**, 350 (2017).
23. M. Hahn, D. Rosenbach, A. Krimalowski, T. Nazarenus, R. Moos, M. Thelakkat, and M. A. Danzer, *Electrochim. Acta*, **344**, 136060 (2020).
24. T. Nazarenus, J. Schneider, L. Hennerici, R. Moos, and J. Kita, *Funct. Mater. Lett.*, **16**, 2350014 (2023).
25. J. Han, A. Vu, J. J. Kim, J. Gim, J. R. Croy, T. H. Lee, and E. Lee, *Chem. Eng. J.*, **481**, 148645 (2024).
26. S. Lang, L. Hennerici, D. Kramer, D. Avadanii, S. Mück, M. Linz, J. Kita, R. Moos, and R. Mönig, *ACS Appl. Mater. Interfaces*, **17**, 56980 (2025).
27. S. Iwasaki, T. Hamanaka, T. Yamakawa, W. C. West, K. Yamamoto, M. Motoyama, T. Hirayama, and Y. Iriyama, *J. Power Sources*, **272**, 1086 (2014).
28. T. Kato, S. Iwasaki, Y. Ishii, M. Motoyama, W. C. West, Y. Yamamoto, and Y. Iriyama, *J. Power Source*, **303**, 65 (2016).
29. M. Linz, F. Bühner, D. Paulus, L. Hennerici, Y. Guo, V. Mereacre, U. Mansfeld, M. Seipenbusch, J. Kita, and R. Moos, *Adv. Mater.*, **36**, 2308294 (2023).
30. I. Kim, T.-H. Nam, K.-W. Kim, J.-H. Ahn, D.-S. Park, C. Ahn, B. S. Chun, G. Wang, and H.-J. Ahn, *Nanoscale Res. Lett.*, **7**, 64 (2012).
31. E. J. Cheng, Y. Kushida, T. Abe, and K. Kanamura, *ACS Appl. Mater. Interfaces*, **14**, 40881 (2022).
32. T. Yamamoto, M. Motoyama, and Y. Iriyama, *J. Jpn. Soc. Powder Powder Metallurgy*, **67**, 200 (2020).
33. S. Muto, Y. Yamamoto, M. Sakakura, H.-K. Tian, Y. Tateyama, and Y. Iriyama, *ACS Appl. Energy Mater.*, **5**, 98 (2022).
34. M. Sakakura, K. Mitsuishi, T. Okumura, N. Ishigaki, and Y. Iriyama, *ACS Appl. Mater. Interfaces*, **14**, 48547 (2022).
35. M. Sakakura, Y. Suzuki, T. Yamamoto, Y. Yamamoto, M. Motoyama, and Y. Iriyama, *Energy Technol.*, **9**, 2001059 (2021).
36. C.-W. Ahn, J.-J. Choi, J. Ryu, B.-D. Hahn, J.-W. Kim, W.-H. Yoon, J.-H. Choi, J.-S. Lee, and D.-S. Park, *J. Power Source*, **272**, 554 (2014).
37. C.-W. Ahn, J.-J. Choi, J. Ryu, B.-D. Hahn, J.-W. Kim, W.-H. Yoon, J.-H. Choi, and D.-S. Park, *Carbon*, **82**, 135 (2015).
38. I. Kim, J. Park, T.-H. Nam, K.-W. Kim, J.-H. Ahn, D.-S. Park, C. Ahn, G. Wang, and H.-J. Ahn, *J. Power Source*, **244**, 646 (2013).
39. C.-W. Ahn, J.-J. Choi, J. Ryu, B.-D. Hahn, J.-W. Kim, W.-H. Yoon, J.-H. Choi, and D.-S. Park, *J. Electrochem. Soc.*, **162**, A60 (2015).
40. D. Paulus, S. Bresch, R. Moos, and D. Schönauer-Kamin, *J. Eur. Ceram. Soc.*, **44**, 116717 (2024).
41. W.-H. Yoon, J. Ryu, J.-J. Choi, B.-D. Hahn, J. H. Choi, B.-K. Lee, J.-H. Cho, and D.-S. Park, *J. Am. Ceram. Soc.*, **93**, 2125 (2010).
42. Y. Nakamura, Y. Matsufuji, and M. Inoue, *J. Phys. Conf. Ser.*, **352**, 12026 (2012).
43. J. Akedo, *J. Therm. Spray. Tech.*, **17**, 181 (2008).
44. J. Exner, T. Nazarenus, D. Hanft, J. Kita, and R. Moos, *Adv. Mater.*, **32**, e1908104 (2020).
45. J. Akedo, N. Minami, K. Fukuda, M. Ichiki, and R. Maeda, *Ferroelectrics*, **231**, 285 (1999).
46. Y. Iriyama, M. Wadaguchi, K. Yoshida, Y. Yamamoto, M. Motoyama, and T. Yamamoto, *J. Power Source*, **385**, 55 (2018).
47. M. Sozak, T. Nazarenus, J. Exner, J. Kita, and R. Moos, *J. Mater. Sci.*, **58**, 10108 (2023).
48. H.-J. Noh, S. Youn, C. S. Yoon, and Y.-K. Sun, *J. Power Source*, **233**, 121 (2013).
49. S.-M. Bak, E. Hu, Y. Zhou, X. Yu, S. D. Senanayake, S.-J. Cho, K.-B. Kim, K. Y. Chung, X.-Q. Yang, and K.-W. Nam, *ACS Appl. Mater. Interfaces*, **6**, 22594 (2014).
50. F. Schipper, E. M. Erickson, C. Erk, J.-Y. Shin, F. F. Chesneau, and D. Aurbach, *J. Electrochem. Soc.*, **164**, A6220 (2017).
51. D. Uxa, E. Hüger, K. Meyer, L. Dörrer, and H. Schmidt, *Chem. Mater.*, **35**, 3307 (2023).
52. I. McClelland, S. G. Booth, N. N. Anthonisamy, L. A. Middlemiss, G. E. Pérez, E. J. Cussen, P. J. Baker, and S. A. Cussen, *Chem. Mater.*, **35**, 4149 (2023).
53. M. Ihrig et al., *J. Power Source*, **482**, 228905 (2021).
54. M. Rosen, M. Finsterbusch, O. Guillon, and D. Fattakhova-Rohlfing, *J. Mater. Chem. A*, **10**, 2320 (2022).
55. C.-L. Tsai et al., *Sustainable Energy Fuels*, **3**, 280 (2019).
56. M. Ihrig et al., *ACS Appl. Mater. Interfaces*, **14**, 11288 (2022).
57. T. Nazarenus, K. Schlesier, S. Biberger, J. Exner, J. Kita, A. Köhler, and R. Moos, *Int. J. Applied Ceramic Tech.*, **19**, 1540 (2022).